Process Safety and Environmental Protection 182 (2024) 1086–1096

Contents lists available at ScienceDirect

Process Safety and Environmental Protection

journal homepage: www.journals.elsevier.com/process-safety-and-environmental-protection

Research on the adsorption mechanism of As by Fe-bearing minerals in coal during high-temperature combustion

Guo-chang Song [a,b], Zhong-wei Li [b], Xing-yu Yang [b], Qiang Song [b,*,1,2]

[a] WISDRI City Environment Protection Engineering CO., LTD, China
[b] Key Laboratory of Thermal Science and Power Engineering of Ministry of Education, Department of Energy and Power Engineering, Tsinghua University, Beijing 100084, China

ARTICLE INFO

Keywords:
As_2O_3
Adsorption
Fe_2O_3
Fe-Si-Al mineral
Coal combustion

ABSTRACT

As can be retained by Fe components in coal during high-temperature combustion, which is beneficial for reducing As emissions. In this study, high-temperature As adsorption experiments were carried out in a fixed-bed experimental system with As model compound and minerals. The adsorption amount of As was much higher when Fe_2O_3, SiO_2, and Al_2O_3 acted together than when they acted alone. As was mainly distributed in the Fe-Si-Al minerals generated by the reaction of the three oxides, for which the Fe_2O_3:SiO_2:Al_2O_3 mass ratio of 1:1:1 was the most favorable, and the maximum adsorption amount of As was 18.2 $mg \cdot g^{-1}$. Density functional theory calculations were carried out for the adsorption of As_2O_3 by Fe_2O_3, SiO_2, Al_2O_3, and $Fe_2Al_4Si_5O_{18}$. $Fe_2Al_4Si_5O_{18}$ had the highest adsorption energy for As_2O_3, indicating the most stable adsorption. As_2O_3 was adsorbed on the Fe and Si sites. The adsorption ability of the Fe site was strengthened in $Fe_2Al_4Si_5O_{18}$ relative to that in Fe_2O_3. The formation of Fe-O-Si and Fe-O-Al in the mineral promoted electron transfer from the adsorbent to As_2O_3 molecule, thereby strengthening adsorption. These results can guide the optimization of coal blending methods and the modification of adsorbents to control As emissions in coal-fired systems.

1. Introduction

During coal combustion, As is easily volatilized into the atmosphere in the form of inorganic As compounds such as As_2O_3. These compounds are highly toxic and undergo bioaccumulation, and thus, they can cause significant harm to human health and the environment (Clarke and Sloss, 1992; Rahman and Singh, 2019; Finkelman, 2004; Arnold, 2023). Since coal combustion is one of the important emission sources of atmospheric As (Tian et al., 2015), it is necessary to control the As emissions from coal-fired plants (U.S. Environmental Protection Agency, 2012; European Union. Directive (EU), 2016). Enhancement of the As enrichment into solid phase in a coal-fired system, followed by the use of a dust collector and a wet desulfurization device to synergistically remove particulate As (Zhao et al., 2017; Wang et al., 2019; Czech et al., 2020) is an effective approach for controlling As emissions.

During high-temperature coal combustion in the coal-fired system, As is retained either owing to its thermal stability or due to the retention by mineral components (Song et al., 2022b, 2022c). After combustion, the flue gas is cooled down, and gaseous As migrates to fly ash due to reactions with minerals, physical adsorption, and condensation (Wierońska-Wiśniewska and Makowska, 2022; Ji et al., 2019; Hu et al., 2021; Xu et al., 2021, 2022). Inhibition of the As release during high-temperature coal combustion by coal blending (Zhao et al., 2021) or mineral addition (Jerzak et al., 2021) can help reduce As emissions, avoid poisoning of Selective catalytic reduction catalyst (Han et al., 2022), and reduce the bioavailability of coal combustion by-products (Han et al., 2022; He et al., 2020). A study of the effects of minerals on As in high-temperature environments can provide guidance for regulatory technologies.

In low-temperature flue gas, As mainly exists in the form of As_2O_5 and will decompose into As_2O_3 when the temperature exceeds 700 ℃ according to the thermodynamic equilibrium calculation results of Shen et al. (2015). Du et al. (2016) compared the Gibbs free energy of different As compounds using quantum chemistry calculations and found that at 1200 ℃, As_2O_3 was more stable than other oxide molecules. Fe oxides can effectively adsorb As_2O_3 at high temperatures

* Correspondence to: Department of Energy and Power Engineering, Tsinghua University, Haidian District, Beijing 100084, China.
E-mail address: qsong@tsinghua.edu.cn (Q. Song).
[1] ORCID: 0000-0002-5484-3594
[2] Researcher ID: U-4938-2019

https://doi.org/10.1016/j.psep.2023.12.039
Received 18 August 2023; Received in revised form 17 November 2023; Accepted 17 December 2023
Available online 28 December 2023

according to previous researches (Song et al., 2021; Fu et al., 2021; Zhang et al., 2016; Zhou et al., 2017). Song et al. (2021) found that Fe_2O_3 shows significant As_2O_3 adsorption in the temperature range of 1000–1300 ℃, with the adsorption capacity decreasing with increasing temperature. Phase characterization results showed that the adsorption product was $FeAsO_4$. It was shown that Fe_3O_4 can also adsorb As (Fu et al., 2021; Zhang et al., 2016). Zhou et al. (2017) conducted co-combustion experiments with coal and minerals using a circulating fluidized bed and found that Fe_2O_3 had a stronger inhibitory effect on As release than $NaNO_3$, KNO_3, Al_2O_3, CaO, and MgO.

The mechanism of As adsorption at the microscopic level can be revealed by quantum chemistry calculations based on density functional theory (DFT). Zhang and Liu (2019) studied the adsorption of As_2O_3 by α- Fe_2O_3 and found that the energy of the system was minimized when As atoms were adsorbed at the O site, and O_2 enhanced the adsorption capacity of the Fe site. However, Wu et al. (2022) found that the most stable adsorption was obtained when the O atoms of As_2O_3 were adsorbed at the O site of the Fe_2O_3 surface. Fu et al. (2021) studied the adsorption of As_2O_3 on the Fe_3O_4 surface via DFT calculations and found that chemical adsorption was dominant and that Fe_3O_4 had more adsorption sites than Fe_2O_3.

The mineral components in coal and ash generally include Fe. According to Seames and Wendt (2007), As content in fly ash particles showed a good correlation with the Ca and Fe contents. Xu et al. (2022) conducted experiments on As_2O_3 adsorption by ash and found through micro composition analysis that As distribution zone on the surface of fly ash overlapped with Ca and Fe. Fu et al. (2021) found that the As enrichment region mainly overlapped with the area of Fe concentration, indicating that As was mainly bound to Fe-bearing minerals. These studies indicate that the Fe component in coal plays a key role in As retention during high-temperature combustion. However, the Fe component in coal can not only be oxidized to iron oxide but can also react with Si and Al components to generate silicoaluminate during high-temperature combustion (Sefidari et al., 2020; Anshits et al., 2020). Wen et al. (2016) used a drop-tube furnace to carry out coal combustion experiments at 1300 ℃ and found that 40–90% of Fe in the ash existed as silicoaluminate with the rest present as oxide. Tian et al. (2015) carried out coal combustion experiments at 1250 ℃ and found that approximately 32% of Fe in ash was present as silicoaluminate. The changes in the morphology of Fe-bearing minerals may lead to changes in the As adsorption capacity (Zha et al., 2018; Cheng et al., 2023; Song et al., 2020a). Exploration of the adsorption mechanism can help enhance the migration of As to the solid phase during coal combustion through fuel blending.

Herein, As adsorption experiments were carried out in a fixed-bed experimental system with As model compounds and mineral oxides (Fe_2O_3, SiO_2, and Al_2O_3). The amounts of As adsorbed by various mineral components were determined, and the adsorption products were analyzed for phase compositions. The impact of the change in the mineral composition on As adsorption was explored. DFT calculations were conducted using the Cambridge Serial Total Energy Package (CASTEP) from Material Studio to compare the structures and energies of As_2O_3 adsorption by Fe_2O_3, SiO_2, Al_2O_3, and $Fe_2Al_4Si_5O_{18}$. Mulliken charge and partial densities of states (PDOS) were analyzed. The mechanism of As_2O_3 adsorption in the presence of Fe, Si, and Al was clarified.

2. Experimental and computational settings

2.1. Experimental settings

Fe_2O_3, SiO_2, and Al_2O_3 were used as adsorbents in this study. The minerals were of analytical grade and were purchased from Shanghai McLean Biochemical Technology Co., Ltd. (Shanghai, China). The As model compound was used as the source of gaseous As, which the mixture of p-aminophenylarsenic acid with cellulose (Song et al., 2023).

As adsorption experiments were carried out in the fixed-bed experimental system as shown in Fig. 1. The detailed instruction to the system was present in our previously published paper (Song et al., 2022c). The reaction gas was the mixture of 79% volume fraction of pure N_2 and 21% volume fraction of pure O_2. The flow rate was 500 mL·min^{-1}. The reactor was heated to 1200 °C, and the reaction gas was introduced. The temperature and atmosphere stabilized after 30 min, and a crucible with 0.3 g of the sample was inserted into the reactor. When the adsorption was finished, the crucible was removed to the cooling area, and the solid products were purged by N_2 and then collected for analysis.

The minerals (150 mg) and As model compounds (150 mg) were used to study As_2O_3 adsorption. Our previous study (Song et al., 2022c) found a negative correlation between the As release ratios at 1200 °C and the Ca, Fe, Si, and Al contents in coal, implying that As retention was achieved under the combined action of the minerals. Herein, the temperature of 1200 °C was selected for the adsorption experiments to further clarify the retention mechanism. The As_2O_3 adsorption amounts obtained under the individual and joint action of Fe_2O_3, SiO_2, and Al_2O_3 were compared, and the influence of the mass ratio of the three mineral components was explored while the total mass of the mineral was kept unchanged. The mass ratios of each mineral under different working conditions were listed in Table 1. A Fourier transform infrared spectrometer (FTIR; Thermo Fisher Scientific Nicolet 6700, USA) was used to detected the concentration of CO_2. It was found that the concentration of CO_2 in the outlet gas reached 0 after 10 min, indicating the complete combustion of the sample. Therefore, the reaction time was set as 10 min

The samples were digested first (Song et al., 2019) and then the As contents in the digestion solution were determined. An inductively coupled plasma emission spectrometer (ICP-OES; Leeman Labs Prodigy 7, USA) was employed for analysis of As content. The analytical method was tested on the standard samples and the recovery rates of As were 99.1%– 100.2%, which proved the accuracy of the method. The adsorption amount of As (mg·g^{-1}) was calculated using Eq. (1).

$$R_{As} = \frac{m_{mi,p} \times C_{mi,p}}{m_{mi,r}} \quad (1)$$

Here, $m_{mi,r}$ is the mass (g) of the clean adsorbents, $m_{mi,p}$ is the mass (g) of the adsorption products, and $C_{mi,p}$ is the As content in adsorption products (mg·g^{-1}).

The phase compositions of the solid products were analyzed with an X-ray diffractometer (XRD; D8 Discover, Bruker, Germany). The micro-area compositions in the adsorption products were analyzed using an electron probe microanalysis (EPMA; JXA8230, JEOL, Japan) system.

2.2. Computational settings

The CASTEP program in Material Studio was selected for the DFT

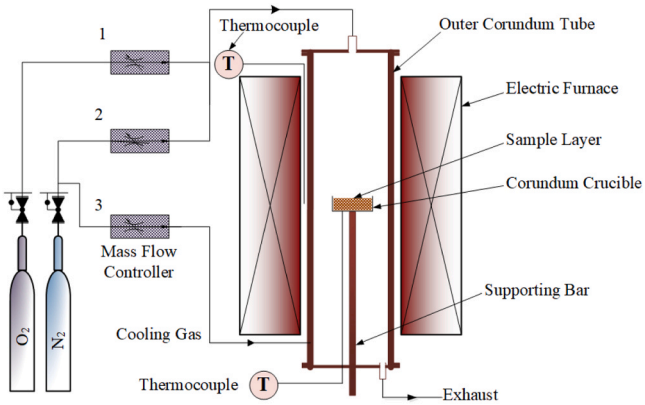

Fig. 1. Structure of the fixed-bed experimental system (Song et al., 2022c).

Table 1
Mass of minerals used for the adsorption experiments (mg).

Sample	Fe_2O_3	SiO_2	Al_2O_3
1	150	0	0
2	0	150	0
3	0	0	150
4	50	100	0
5	50	0	100
6	0	75	75
7	50	75	25
8	50	67	33
9	50	50	50
10	50	33	67
11	50	25	75
12	30	60	60
13	70	40	40
14	100	25	25

calculations (Clark et al., 2005). The methods (Burke et al., 1996; Vanderbilt, 1990; Press et al., 1996) and the convergence criteria were the same as in our previous study (Song et al., 2023). Spin-polarized calculations were used. The adsorption of As_2O_3 by $Fe_2Al_4Si_5O_{18}$, which is a typical Fe-bearing aluminosilicate mineral, was investigated in this study. The optimized cell parameters were: a = 17.440 Å, b = 9.886 Å, c = 9.359 Å. The relative deviation from the experimental data of Haefeker et al. (2014) was within 2%, proving that the method was reliable. The dominant crystal plane of $Fe_2Al_4Si_5O_{18}$, namely the (1 1 0) surface, was used to build slab models (Son et al., 2019). The vacuum region was 15 Å. The layer of atoms on the surface was relaxed, and the rest of atoms were fixed. Convergence tests were conducted and the results are shown in Tables S1 and S2. It was found that when the cut-off energy was 490 eV or higher, the change in energy was within 1%. Therefore, a cut-off energy of 490 eV was chosen. Similarly, a 1 × 1 × 1 k-point mesh was used for the calculations. The slab models with different layer and horizontal planes were built. The adsorption energy E_{ad} (kJ·mol^{-1}) was calculated by Eq. (2):

$$E_{ad} = E_{product} - E_{adsorbent} - E_{adsorbate} \quad (2)$$

where $E_{product}$, $E_{adsorbent}$, and $E_{adsorbate}$ are the energies (kJ·mol^{-1}) of the adsorption product, adsorbent, and adsorbate, respectively.

When the relative deviation of E_{ad} of slab models with different sizes was within 1%, the calculation accuracy was enough. According to the results of Table 2, a two-layer slab model with a 1 × 1 horizontal plane was chosen (Fig. 2). The Fe_2O_3 (0 0 1), SiO_2 (1 0 0), and Al_2O_3 (0 0 1) slab models were built according to previous studies (Yu et al., 2021, 2022). The chain form of the As_2O_3 molecule was chosen because its Gibbs energy was lower than those of the other types of As molecules at temperatures above 1173 °C according to Ling et al. (2021).

3. Results and discussion

3.1. As_2O_3 adsorption characteristics by different mineral components

The amounts of As adsorbed after the co-combustion of the mineral (150 mg) and the As model compound (150 mg) at 1200 °C for 10 min are presented in Fig. 3. It can be observed that the adsorption capacity of the three mineral oxides acting alone on As was relatively weak. The amount of As adsorbed by Fe_2O_3 was 0.6 mg·g^{-1}, while for both SiO_2 and Al_2O_3, the adsorption amounts were lower than 0.2 mg·g^{-1}. When

Table 2
E_{ad} of As_2O_3 adsorption on m layer – n × n surface slab models (kJ·mol^{-1}).

n		1	2	3
m	1	-552.44	-587.99	-579.13
	2	-760.52	-768.01	-767.55
	3	-759.44	-761.83	-762.08

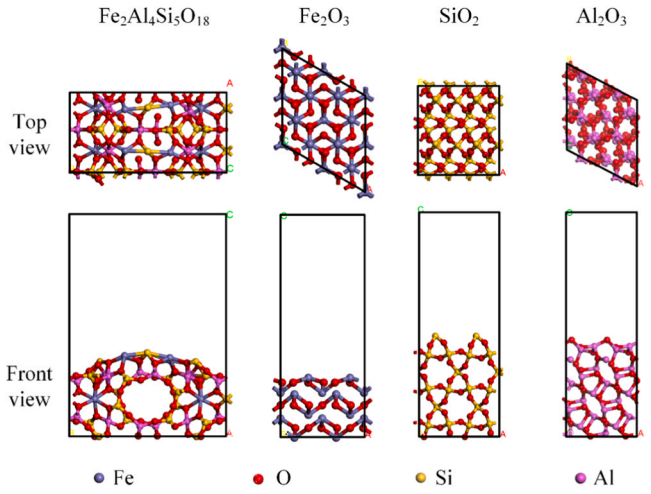

Fig. 2. Structures of $Fe_2Al_4Si_5O_{18}$, Fe_2O_3, SiO_2, and Al_2O_3 slab models.

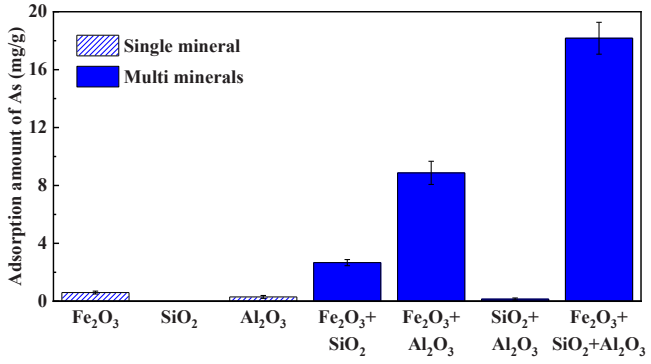

Fig. 3. Adsorption amount of As by different mineral components.

different mineral oxides acted together, the adsorption amount of As changed. After mixing Fe_2O_3 with SiO_2 and Al_2O_3 respectively and the mass ratio was 1:2, the amount of adsorbed As increased significantly to 2.7 mg·g^{-1} and 8.9 mg·g^{-1}, respectively. By contrast, under the joint action of SiO_2 and Al_2O_3, the adsorption amount of As was only 0.1 mg·g^{-1}. Mixing of the three oxides in a mass ratio of 1:1:1 resulted in the As adsorption amount of 18.2 mg·g^{-1}. This indicates that SiO_2, Al_2O_3, and Fe_2O_3 enhanced the adsorption of As_2O_3 through a synergistic coupling effect.

For the Fe_2O_3 +SiO_2 +Al_2O_3 mineral with the highest As adsorption amount in Fig. 3, the effect of mineral component ratios on As_2O_3 adsorption was further investigated. The ratio of SiO_2 and Al_2O_3 was changed, while the total mass of the minerals and the mass fraction of Fe_2O_3 remained unchanged with the obtained As adsorption amount shown in Fig. 4(a). When the SiO_2:Al_2O_3 ratio was below 1:1, As adsorption amount increased with the increase of SiO_2:Al_2O_3 ratio. When the SiO_2:Al_2O_3 ratio was above 1:1, As adsorption amount showed an opposite trend. The maximum adsorption amount of As was 18.2 mg·g^{-1} for SiO_2:Al_2O_3 = 1:1. Subsequently, the fraction of Fe_2O_3 was changed, while the total mass of the minerals and the SiO_2:Al_2O_3 ratio of 1:1 remained unchanged with the obtained As adsorption amount shown in Fig. 4(b). With increasing Fe_2O_3 fraction, As adsorption first increased and then decreased, and reached the maximum value for Fe_2O_3:(SiO_2 +Al_2O_3) = 1:2. This is because the addition of a certain amount of Si and Al to Fe_2O_3 can enhance As adsorption through a coupling effect; however, the adsorption on the Si and Al components can be ignored. Fe is the effective component for As adsorption when multiple minerals act together. Therefore, when the mass fraction of Fe_2O_3 further decreased, the adsorption amount of As also decreased.

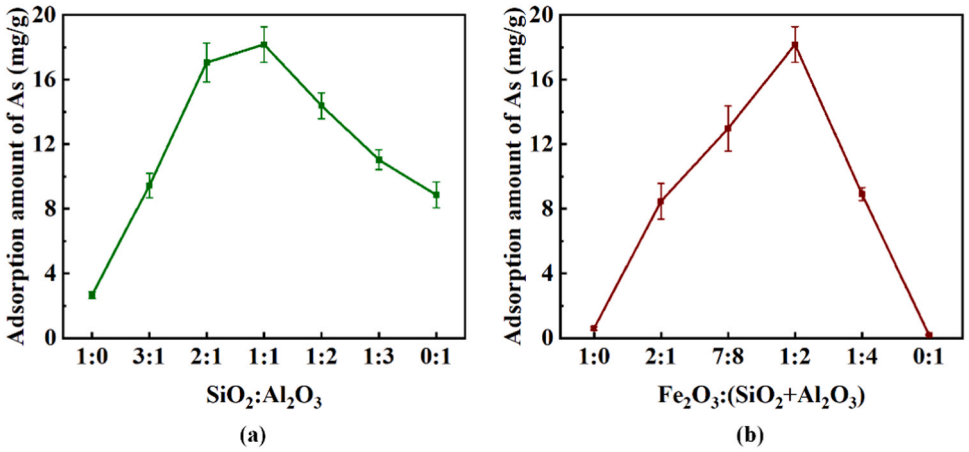

Fig. 4. Adsorption amount of As by different mineral components.

Fig. 5(a) and (b) show the microstructure of the adsorption products under the joint action of Fe_2O_3, SiO_2, and Al_2O_3 and the results of the surface scan analysis of the As element, respectively. It can be observed that As was not uniformly distributed in the product, but it was rather enriched in some regions. Component analysis was conducted on 11 points in the As-enriched area, with the results shown in Fig. 5(c). The Fe, Si, and Al contents in this area were significant, indicating that As was bound to Fe-Si-Al minerals. The main form of such mineral was cordierite ($Fe_2Al_4Si_5O_{18}$), according to Fig. 5(d).

When Fe_2O_3, SiO_2, and Al_2O_3 acted alone, their adsorption capacity for As was lower. By contrast, when they acted together, As adsorption increased significantly, reaching the maximum value at the mass ratio of 1:1:1. This phenomenon suggests that the combined action of Fe, Si, and Al minerals strengthened As adsorption. The micro composition and phase analysis results of the product indicate that the adsorbed As was mainly bound to Fe-Si-Al minerals (such as $Fe_2Al_4Si_5O_{18}$). When the ratio of Fe_2O_3:SiO_2:Al_2O_3 was 1:1:1, it was most favorable for the generation of Fe-Si-Al minerals, and thus the adsorption amount of As reached the highest. Therefore, in Section 3.2, the adsorption structures of As_2O_3 on Fe_2O_3, SiO_2, Al_2O_3, and $Fe_2Al_4Si_5O_{18}$ surfaces are compared at the micro-scale to explore the adsorption enhancement mechanism.

3.2. *Adsorption mechanism of As_2O_3 by Fe_2O_3, SiO_2, Al_2O_3, and $Fe_2Al_4Si_5O_{18}$*

After structure optimization, the structure of As_2O_3 adsorbed on the

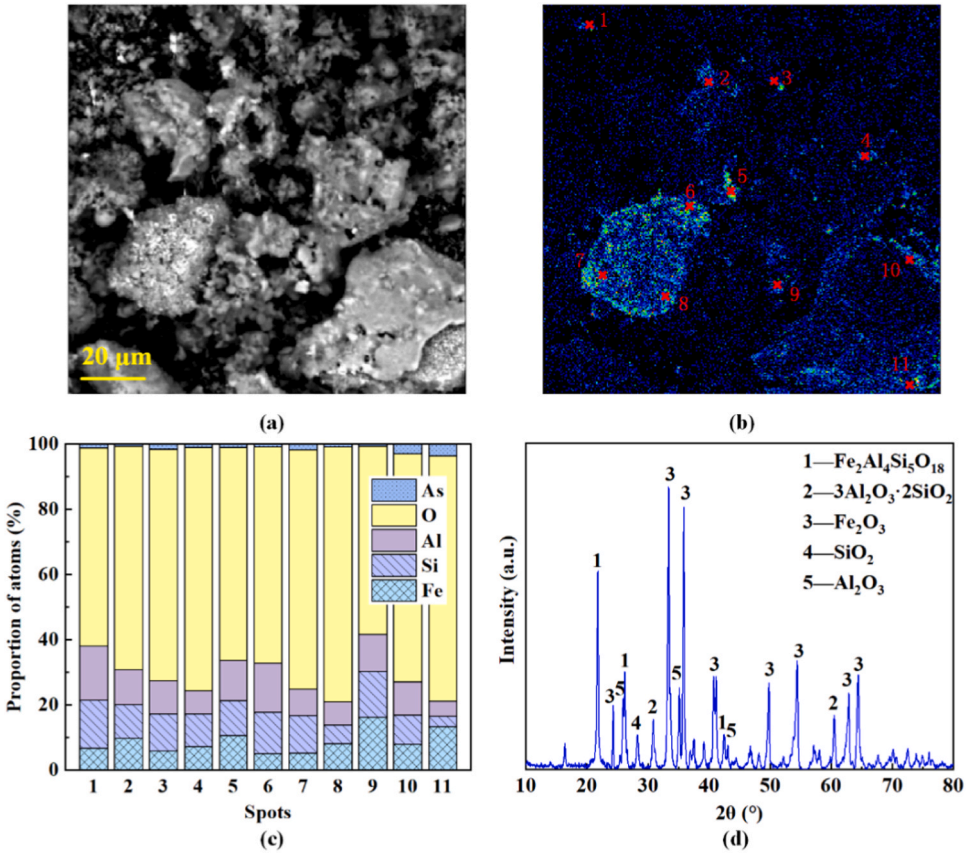

Fig. 5. EPMA and XRD results of adsorption products of Fe_2O_3 + SiO_2 + Al_2O_3.

Fe_2O_3 (0 0 1) surface is shown in Fig. 6(a). The adsorption sites on the Fe_2O_3 (0 0 1) surface included Fe and O sites. Upon adsorption, the As (1)-O(2) bond in the As_2O_3 molecule broke, and the As(1)-O(2) distance increased from 1.808 Å to 3.098 Å. The As atom was bound to the O site on the surface of the adsorbent with a bond distance of 1.999 Å. The three O atoms were bound to the Fe sites, with bond lengths ranging from 1.893 to 1.932 Å. The bonding mechanism during the adsorption can be analyzed through the examination of partial density of states (PDOS). Fig. 6(b) shows the PDOS of Fe(1) and O(1) atoms after adsorption, and it can be observed that the two PDOS overlapped at − 6.5, − 3.8, and − 2.5 eV, implying the generation of Fe-O bonds. Fig. 6(c) shows that the PDOS for the p-orbital electron of O(4) and As(1) atoms overlapped at − 10.9, − 6.9, − 4.5, 1.7, 2.5, 3.9, and 4.4 eV, indicating the formation of As-O bonds. Fig. 6(d) shows that the PDOS of the Fe(2) and O(2) electrons overlapped at − 10.2, − 6.0, − 3.9, − 2.5, and 1.3 eV, and Fig. 6(e) shows that the PDOS of the Fe(3) and O(3) electrons overlapped at − 10.1, − 4.7, − 1.6, and 1.1 eV, indicating the formation of Fe-O bonds at the Fe(2) and Fe(3) sites.

The structure of the As_2O_3 molecule adsorbed on the SiO_2 (1 0 0) surface is shown in Fig. 7(a). Si was the adsorption site. The O atoms at both ends of As_2O_3 are bound to Si on the surface of the adsorbent, with bond distances of 1.566 and 1.639 Å. Fig. 7(b) shows the PDOS of the Si (1) and O(1) atoms, and it can be observed that their p-orbital PDOS overlapped at − 7.1, − 5.4, − 3.2, − 1.0, and 5.1 eV. It can be observed from Fig. 7(c) that the p-orbital PDOS of the Si(2) and O(3) atoms overlapped at − 4.8, − 3.2, − 2.4, 0.9, and 2.5 eV. These results indicate

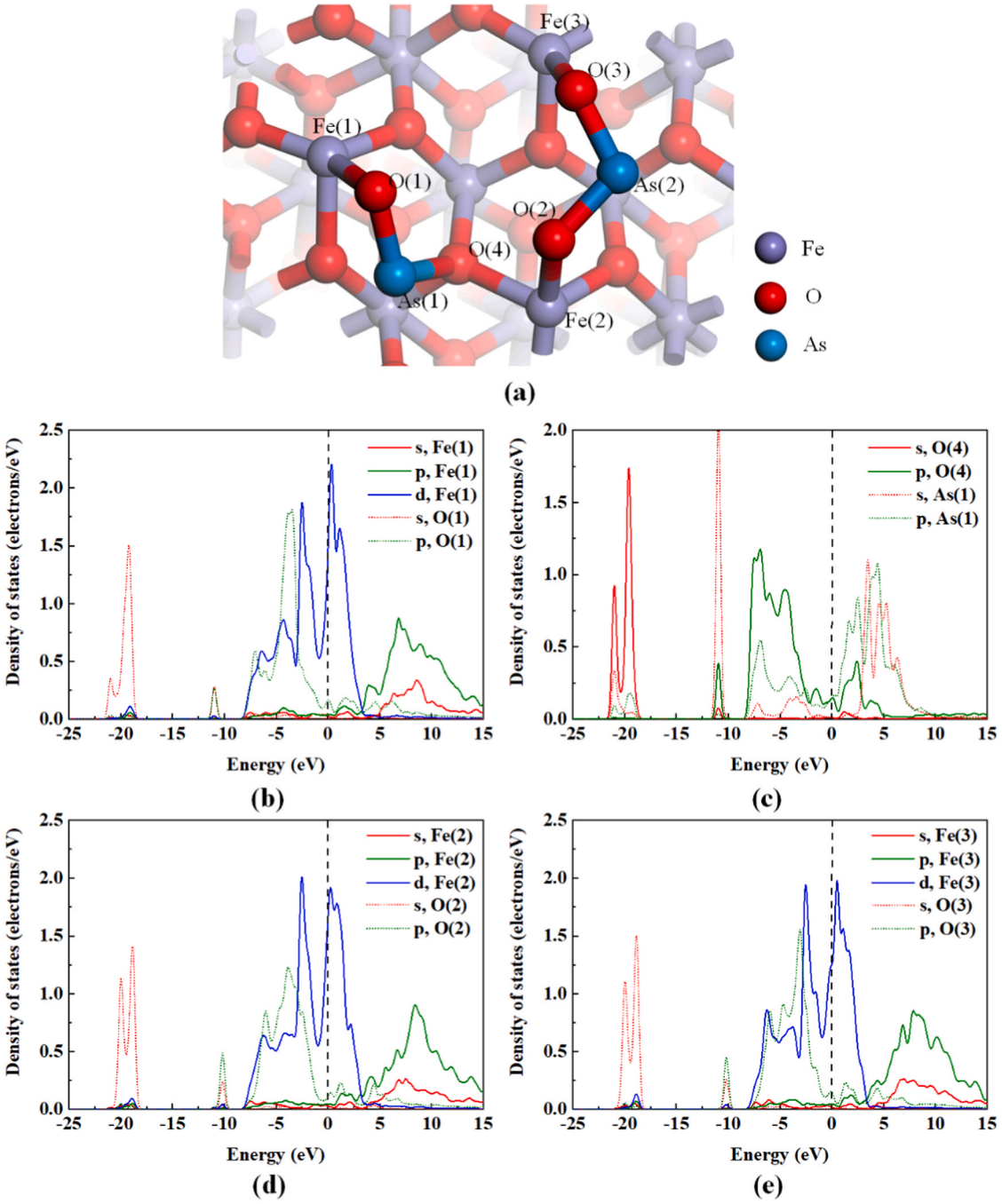

Fig. 6. (a) Structure of As_2O_3 adsorbed by Fe_2O_3; (b) PDOS of Fe(1) and O(1) atoms; (c) PDOS of O(4) and As(1) atoms; (d) PDOS of Fe(2) and O(2) atoms; (e) PDOS of Fe(3) and O(3) atoms.

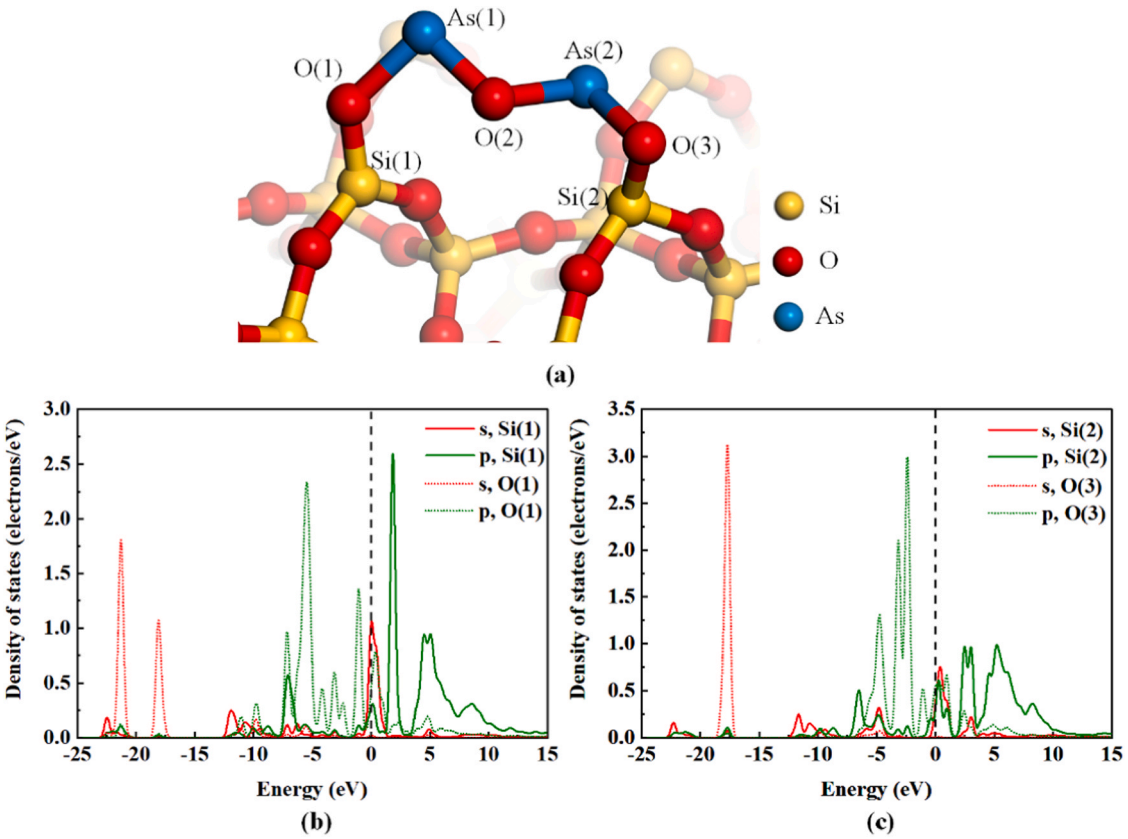

Fig. 7. (a) Structure of As_2O_3 adsorbed by SiO_2; (b) PDOS of Si(1) and O(1) atoms; (c) PDOS of Si(2) and O(3) atoms.

that Si-O bonds were formed at both Si(1) and Si(2) sites.

The structure of the As_2O_3 molecule adsorbed on the Al_2O_3 (0 0 1) surface is shown in Fig. 8(a). The adsorption sites include Al and O sites. The O atoms at both ends of As_2O_3 are bound to Al on the surface of the adsorbent, with a bond distance of 1.795 Å, and the two As atoms are bound to the surface O, with bond distances of 1.869 and 1.895 Å. Fig. 8 (b) shows the PDOS of the Al(1) and O(1) atoms, where the p-orbital PDOS of the two atoms overlapped at − 16.7, − 3.6, − 1.9, 2.5, and 6.8 eV. Fig. 7(c) shows that the p-orbital PDOS of the Al(2) and O(3) atoms overlapped at − 3.0, − 1.3, and 3.9 eV. These results indicate that Al-O bonds were formed at both Al(1) and Al(2) sites. Fig. 7(d) shows that the p-orbital PDOS of the O(5) and As(1) atoms overlapped at − 11.8, − 6.2, − 2.9, 1.4, and 2.4 eV, and Fig. 7(e) shows that the p-orbital PDOS of the O(6) and As(2) atoms overlapped at − 1.9, − 0.5, 1.4, and 2.4 eV, indicating that As-O covalent bonds were formed at both locations.

The adsorption of As_2O_3 on different sites of the $Fe_2Al_4Si_5O_{18}$ (1 1 0) surface were calculated, and 72 kinds of adsorption sites were obtained. Among them, the most stable structure is shown in Fig. 9(a). After adsorption, As_2O_3 molecules undergo deformation, resulting in the breaking of the As-O bonds and the formation of two functional groups, namely AsO and AsO_2. The As(1)-O(1) and As(1)-O(2) bond lengths in the AsO_2 group increased from 1.621 and 1.808 Å to 1.852 and 1.976 Å, respectively. The As(2)-O(3) bond lengths in the AsO group increased from 1.621 Å to 1.750 Å, and the O-As-O bond angle increased from 108.2° to 101.9°. This indicates that there was a strong interaction between the $Fe_2Al_4Si_5O_{18}$ (1 1 0) surface and the As_2O_3 molecules.

The two atoms of the AsO group were located at the Fe sites on the surface, while the AsO_2 group was connected through the bonding of its two O atoms to the surface Al atom. After adsorption, the distance between O(1) and Si(3) was 1.747 Å, that between O(2) and Si(4) was 1.679 Å, that between O(3) and Fe(4) was 1.840 Å, and that between As (2) and Fe(5) was 2.306 Å. The PDOS analysis results presented in Fig. 9 (b)–(e) show that the PDOS of Fe(4) and O(3) overlapped at − 10.5, − 5.9, − 4.7, and − 1.7 eV, while the PDOS of Fe (5) and As (2) overlapped at − 4.7, − 2.7, 0.6, and 2.2 eV. The p-orbitals of Si(3) and O(1) overlapped at − 7.4, − 6.2, − 1.4, and − 0.3 eV, and the p-orbitals of Si (4) and O(2) overlapped at − 11.5, − 7.2, − 0.5, and 3.1 eV. These results indicate the formation of Fe-O, Fe-As, and Si-O bonds during adsorption.

As_2O_3 adsorption sites include the Fe and O sites on the Fe_2O_3(0 0 1) surface, Si sites on the SiO_2 (1 0 0) surface, Al and O sites on the Al_2O_3(0 0 1) surface, and Fe and Si sites on the $Fe_2Al_4Si_5O_{18}$ (1 1 0) surface. PDOS analysis results showed that new chemical bonds were formed at each site. Section 3.3 reveals the coupling mechanism of the Fe, Si, and Al enhancement of As_2O_3 adsorption by comparing the adsorption energy, charge transfer, and bonding strength of As_2O_3 adsorption by different minerals.

3.3. *Comparative analysis of As_2O_3 adsorption strength by different adsorbents*

As shown in Table 3, the As_2O_3 adsorption energies on different mineral surfaces are in the order of $Fe_2Al_4Si_5O_{18}$ (-770.96 kJ·mol^{-1}) > Fe_2O_3(-325.65 kJ·mol^{-1}) > Al_2O_3 (-263.73 kJ·mol^{-1}) > SiO_2 (-251.13 kJ·mol^{-1}). $Fe_2Al_4Si_5O_{18}$ had the highest adsorption strength for As_2O_3, so the generation of the $Fe_2Al_4Si_5O_{18}$ Fe-Si-Al mineral increased the As adsorption amount, as shown in Section 3.1.

The Mulliken charges of the As_2O_3 molecules before and after adsorption by different minerals are compared in Fig. 10. The Mulliken charge of As_2O_3 changed from 0 to a negative value upon adsorption, indicating electron transfer from the adsorbent surface to As_2O_3 in the adsorption process. In particular, As_2O_3 adsorbed by $Fe_2Al_4Si_5O_{18}$ obtained the most electrons (1.42 e), which also confirmed its highest adsorption strength. The Mulliken charge of As_2O_3 in the Fe_2O_3 adsorption structure was the second-highest at − 1.28 e. The As_2O_3

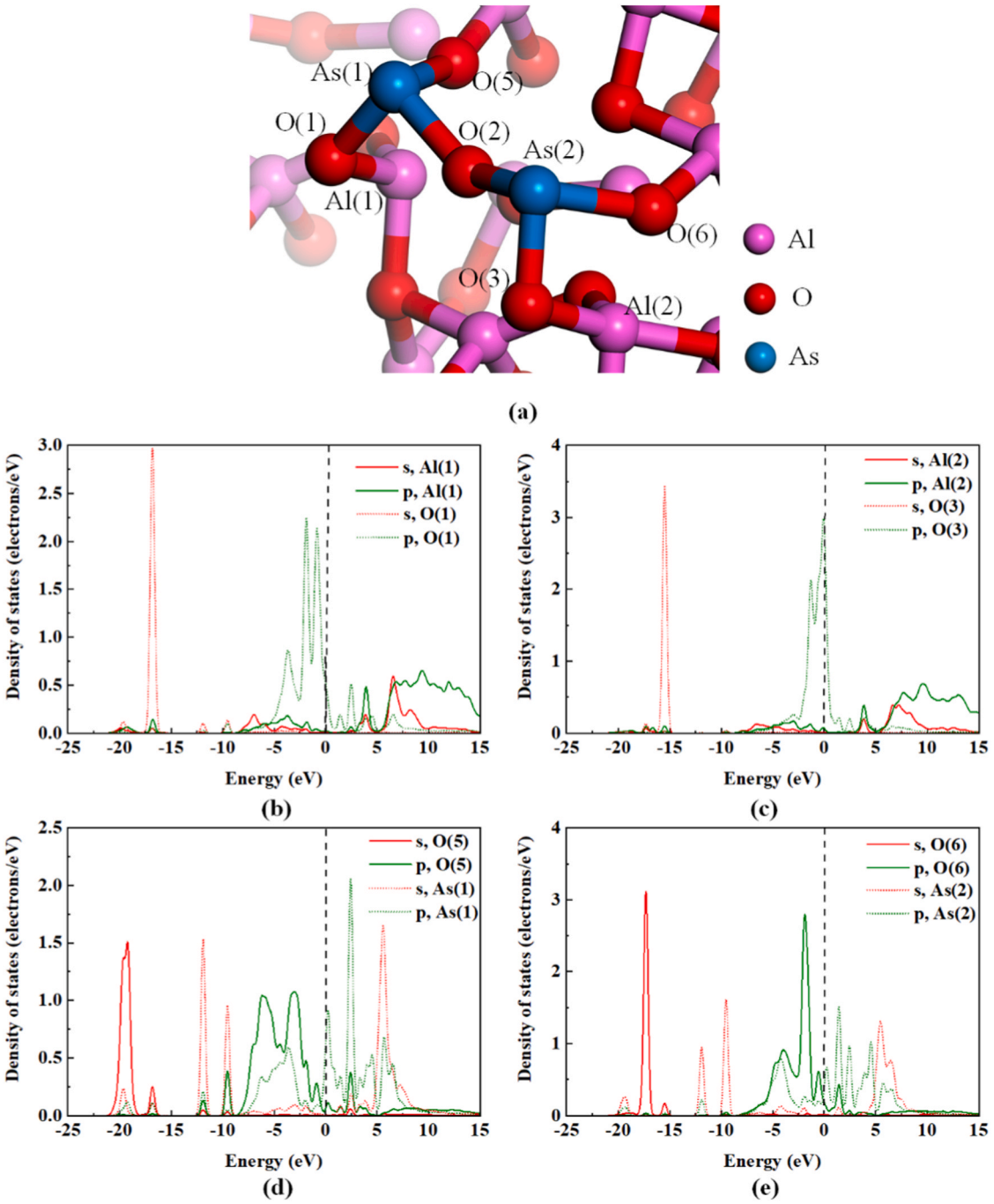

Fig. 8. (a) Structure of As_2O_3 adsorbed by Al_2O_3; (b) PDOS of Al(1) and O(1) atoms; (c) PDOS of Al(2) and O(3) atoms; (d) PDOS of O(5) and As(1) atoms; (e) PDOS of O(6) and As(2) atoms.

adsorbed by Al_2O_3 and SiO_2 showed weaker electron transfer, with the Mulliken charge values of 0.26 e and 0.16 e, respectively.

In the $Fe_2Al_4Si_5O_{18}$ adsorption structure, As(1) atoms did not directly bind to the adsorption site, while As(2) atoms were bound to the Fe site. The Mulliken charge of both atoms decreased more significantly than those of the other atoms, decreasing from 1.26 e to 0.63 e. In the Fe_2O_3 and SiO_2 adsorption structures, the Mulliken charges of As(1) and As(2) decreased by 0.39–0.58 e and 0.04–0.06 e, respectively, while the charges of the As atoms in the Al_2O_3 adsorption structure increased by 0.01–0.03 e. The As atoms in these structures were bound to the adsorbent surface through bridge O. It is speculated that the maximum change in the As atomic charge in the $Fe_2Al_4Si_5O_{18}$ adsorption structure may be related to the adsorption strength of the Fe and Si sites. In addition, the charge variation of the O(1) and O(3) atoms in the $Fe_2Al_4Si_5O_{18}$ adsorption structure was lower than that of other structures, while the charge of O(2) was higher than that of Fe_2O_3 and Al_2O_3 and lower than that of SiO_2.

The adsorption sites of $Fe_2Al_4Si_5O_{18}$ included Fe and Si, and new Fe-O and Si-O bonds were generated after adsorption. These two adsorption sites are also present in Fe_2O_3 and SiO_2, respectively. Therefore, to analyze bonding strength, the bond lengths and population in different adsorption structures are compared in Table 4. It is observed that in the Fe_2O_3 adsorption structure, the Fe-O bond length between the As_2O_3 molecules and the surface was 1.893–1.912 Å; while in the $Fe_2Al_4Si_5O_{18}$ adsorption structure, the Fe-O bond length was 1.840 Å. A shorter bond length implies more stable bonding, and a higher population indicates a

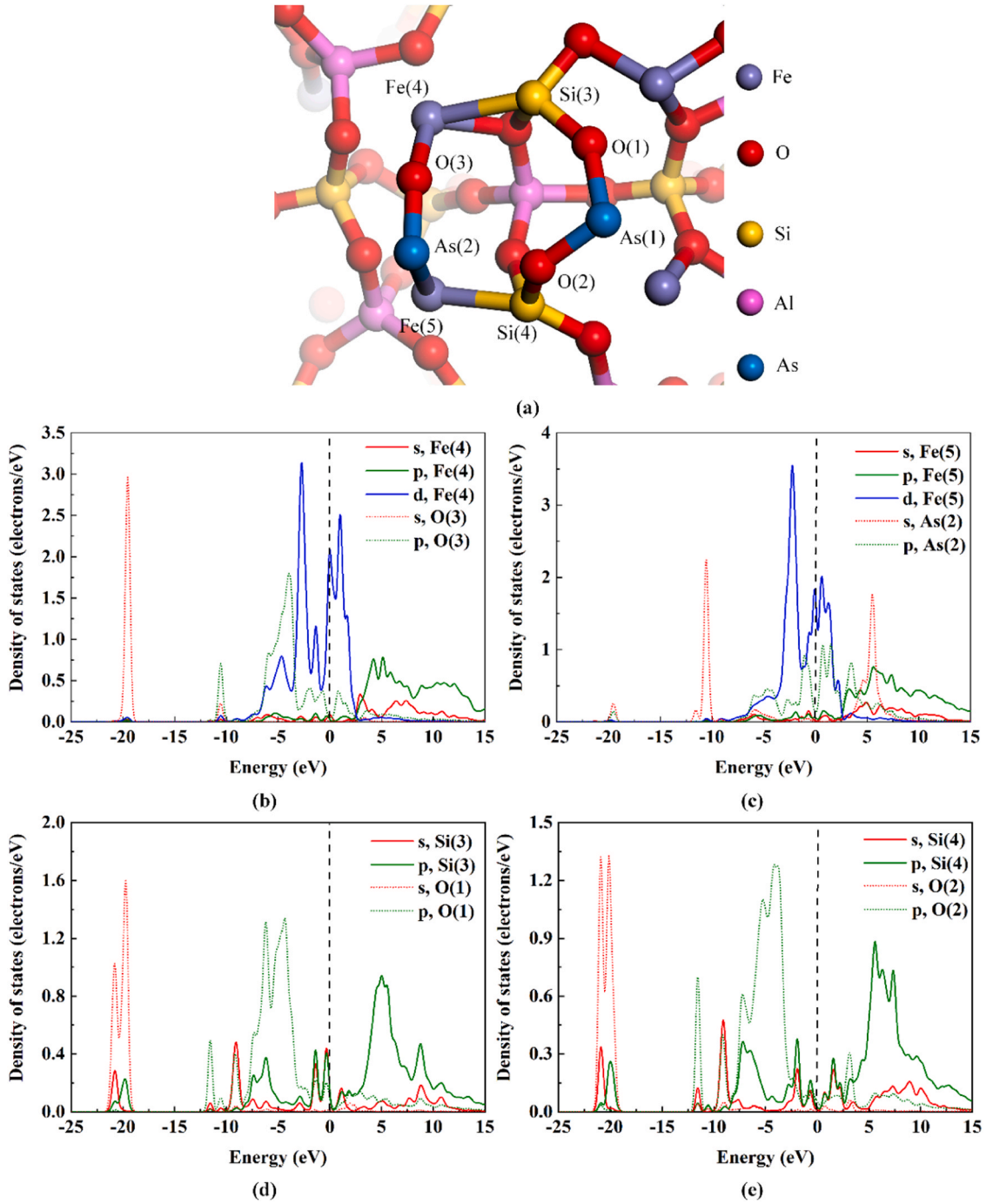

Fig. 9. (a) Structure of As_2O_3 adsorbed by $Fe_2Al_4Si_5O_{18}$; (b) PDOS of Fe(4) and O(3) atoms; (c) PDOS of Fe(5) and As(2) atoms; (d) PDOS of Si(3) and O(1) atoms; (e) PDOS of Si(4) and O(2) atoms.

Table 3
E_{ad} of As_2O_3 adsorption by different adsorbents (kJ·mol^{-1}).

Adsorbents	$Fe_2Al_4Si_5O_{18}$	Fe_2O_3	Al_2O_3	SiO_2
E_{ad}	-770.96	-325.65	-263.73	-251.13

greater overlap of electron orbitals.

The DOS of Fe-O bond of Fe_2O_3 and $Fe_2Al_4Si_5O_{18}$ adsorbing As_2O_3 are shown in Fig. 11. It can be observed that compared with the As_2O_3 adsorption by Fe_2O_3, the molecular orbital and anti-bonding molecular orbital of Fe-O(As_2O_3) bonding in the As_2O_3 adsorption by $Fe_2Al_4Si_5O_{18}$ structure moved to lower and higher energy levels, respectively. The energy band was wider, indicating that the bonding was more stable. The DOS analysis results for the adsorbents indicate that the energy gap of Fe in $Fe_2Al_4Si_5O_{18}$ (1.1 eV) was lower than that of Fe in Fe_2O_3 (3.2 eV) so that the outer electrons were more prone to undergo transitions. Therefore, the adsorption capacity of Fe sites is enhanced.

In the $Fe_2Al_4Si_5O_{18}$ adsorption structure, the Si-O bond length for the bond between As_2O_3 molecules and the surface ranges from 1.679–1.747 Å, with a bond population of 0.43–0.51. In the SiO_2 adsorption structure, the Si-O bond length is 1.566 Å, and the bond population is 0.66. This indicates that a weaker Si-O bond was formed when $Fe_2Al_4Si_5O_{18}$ adsorbed As_2O_3. Fig. 10 shows that the reduction in the Mulliken charge of the O(1) and O(3) atoms in the $Fe_2Al_4Si_5O_{18}$

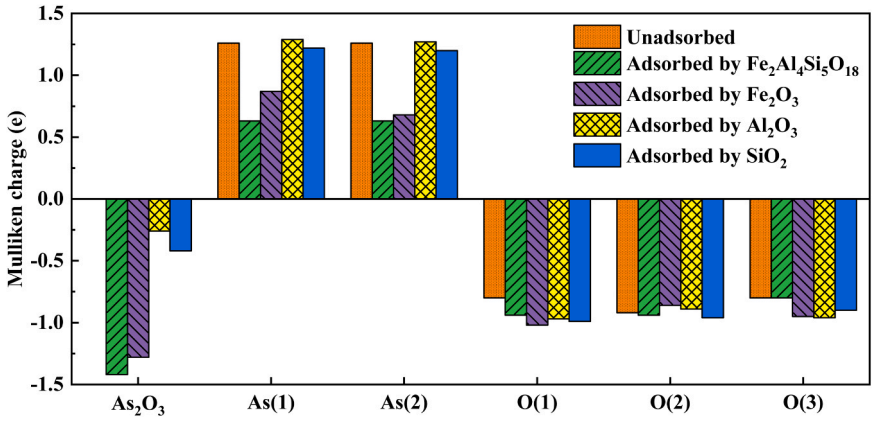

Fig. 10. Mulliken charge of As_2O_3 molecule and each atom.

Table 4
Length and population of Fe-O(As_2O_3) and Si-O(As_2O_3) bonds.

Bond	Adsorbent	Length (Å)	Population
Fe-O(As_2O_3)	$Fe_2Al_4Si_5O_{18}$	1.840	0.43
	Fe_2O_3	1.893, 1.910, 1.912	0.31, 0.34, 0.39
Si-O(As_2O_3)	$Fe_2Al_4Si_5O_{18}$	1.679, 1.747	0.51, 0.43
	SiO_2	1.566, 1.639	0.66, 0.49

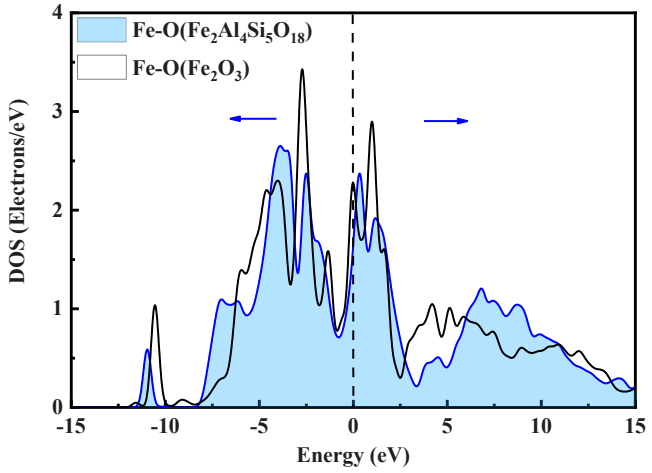

Fig. 11. Mulliken charge of As_2O_3 molecule and each atom.

adsorption structure (0.14 e) was significantly lower than that in the SiO_2 adsorption structure (0.29 e), implying that fewer electrons were transferred. Therefore, the adsorption capacity of Si sites for As_2O_3 was weakened in $Fe_2Al_4Si_5O_{18}$.

In summary, the adsorption energy of As_2O_3 on the $Fe_2Al_4Si_5O_{18}$ surface was higher than that on the Fe_2O_3, Al_2O_3, and SiO_2 surfaces, while the Mulliken charge difference before and after adsorption was larger, indicating more stable adsorption. The Fe and Si sites on the surface of $Fe_2Al_4Si_5O_{18}$ participate in the adsorption of As_2O_3, and these two sites also exist on the Fe_2O_3 and SiO_2 surfaces. Through comparative analysis of bonding strengths, it was found that the Fe-O(As_2O_3) generated after adsorption by $Fe_2Al_4Si_5O_{18}$ was more stable, indicating that the adsorption ability was strengthened on the Fe sites. However, the adsorption capacity of the Si sites was weakened. Therefore, the combined action of Fe, Si, and Al promotes the electron transfer from $Fe_2Al_4Si_5O_{18}$, particularly from the Fe site, to the As_2O_3 molecules, thereby strengthening adsorption.

These calculation results can support the experimental results. In the high-temperature adsorption experiments, the adsorption amounts of As for Fe_2O_3, SiO_2, and Al_2O_3 acting alone and together were determined. When the minerals acted alone, As_2O_3 was adsorbed on the Fe and O sites on the Fe_2O_3 (0 0 1) surface, Si site on the SiO_2 (1 0 0) surface, and Al and O sites on the Al_2O_3 (0 0 1) surface. When these minerals acted together, Fe-Si-Al minerals (such as $Fe_2Al_4Si_5O_{18}$) were generated, and the As_2O_3 adsorption on the Fe site was enhanced. The stronger the adsorption, the higher the adsorption amount. When the ratio of these three minerals was close to 1:1:1, it was most favorable for the generation of Fe-Si-Al minerals. Therefore, the adsorption amount reached the highest. These results indicate that during high-temperature combustion of coal, the Fe component in the coal reacts with Si and Al to generate silicoaluminate, enhancing the As_2O_3 adsorption capacity, and As is thus retained in the solid phase.

4. Conclusions

The adsorption characteristics of As for Fe_2O_3, SiO_2, and Al_2O_3 acting alone and together were determined. When the three minerals acted alone, lower adsorption amounts of As were obtained, whereas the As adsorption amount increased significantly when they acted together. For the same total mineral mass, the amount of As adsorbed by minerals showed a trend of first increasing and then decreasing with the increase in any mineral oxide mass fraction, reaching a maximum value of 18.2 $mg \cdot g^{-1}$ for the ratio of the three minerals of 1:1:1. The phase composition of the adsorption products mainly included $3Al_2O_3 \cdot 2SiO_2$, $Fe_2Al_4Si_5O_{18}$, and the three types of mineral oxides. Micro-area composition analysis showed that As was mainly distributed in Fe-Si-Al minerals, namely $Fe_2Al_4Si_5O_{18}$. Formation of Fe-Si-Al minerals at high temperatures was most favorable when the mass fractions of Fe_2O_3, SiO_2, and Al_2O_3 were equal so that the highest adsorption capacity for As was obtained at the Fe_2O_3:SiO_2:Al_2O_3 ratio of 1:1:1.

The adsorption mechanism of As_2O_3 on Fe_2O_3, SiO_2, Al_2O_3, and $Fe_2Al_4Si_5O_{18}$ surfaces was explored, and the origin of the enhanced adsorption was revealed. As_2O_3 was bound to the Fe and O sites on the Fe_2O_3 (0 0 1) surface to form Fe-O and O-As bonds, Si sites on the SiO_2 (1 0 0) surface to form Si-O bonds, Al and O sites on the Al_2O_3 (0 0 1) surface to form Al-O and O-As bonds, and Fe and Si sites on the $Fe_2Al_4Si_5O_{18}$ (1 1 0) surface to form Fe-O, Fe-As, and Si-O bonds. The adsorption energy of As_2O_3 on the surface of $Fe_2Al_4Si_5O_{18}$ was higher than those on the Fe_2O_3, SiO_2, and Al_2O_3 surfaces, indicating a more stable adsorption structure. This was ascribed to the joint action of Fe, Si, and Al promoting the electron transfer from $Fe_2Al_4Si_5O_{18}$, and particularly the Fe site, to the As_2O_3 molecules, rendering the Fe-O (As_2O_3) bond generated after adsorption more stable, and thereby strengthening adsorption.

During high-temperature coal combustion, the Fe, Si, and Al components reacted to form Fe-Si-Al mineral, enhancing the As_2O_3

adsorption capacity and thus retaining As in the solid phase. The results of this study provide theoretical support for the optimization of control strategies for As emission. Blending coals with difference in the contents of Fe, Si, and Al and promoting the generation of Fe-Si-Al mineral would enhance the retention of As. Modifying Fe-based mineral adsorbents with Si and Al can also enhance their adsorption ability in future studies.

Declaration of Competing Interest

The authors declare that they have no known competing financial interests or personal relationships that could have appeared to influence the work reported in this paper.

Acknowledgments

This work was financially supported by the China National Key Research and Development Program (2022YFB4100201) and the Fundamental Research Funds for the Central Universities of China (2022ZFJH004).

Appendix A. Supporting information

Supplementary data associated with this article can be found in the online version at doi:10.1016/j.psep.2023.12.039.

References

Anshits, N.N., Fedorchak, M.A., Fomenko, E.V., Mazurova, E.V., Anshits, A.G., 2020. Composition, structure, and formation routes of blocklike ferrospheres separated from coal and lignite fly ashes. Energy Fuels 34, 3743–3754.
Arnold, B.J., 2023. A review of element partitioning in coal preparation. Int. J. Coal Geol. 274, 104296.
Burke, K., Ernzerhof, M., Perdew, J.P., 1996. Generalized gradient approximation made simple. Phys. Rev. Lett. 77, 3865–3868.
Cheng, H.Q., Huang, Y.J., Zhu, Z.C., Yu, M.Z., Xu, W.T., Li, Z.Y., Xiao, Y.X., 2023. Adsorption of cadmium vapor by calcium-based adsorbents in simulated flue gas: experimental and density functional theory studies. Appl. Surf. Sci. 614, 156057.
Clark, S.J., Segall, M.D., Pickard, C.J., Hasnip, P.J., Probert, M.I., Refson, K., Payne, M.C., 2005. First principles methods using CASTEP. Cryst. Mater. 220, 567–570.
Clarke, L.B., Sloss, L.L., 1992. Trace elements - emissions from coal combustion and gasification. IEA Coal Res. 49, 36–37.
Czech, T., Marchewicz, A., Sobczyk, A.T., Krupa, A., Jaworek, A., Śliwiński, Ł., Rosiak, D., 2020. Heavy metals partitioning in fly ashes between various stages of electrostatic precipitator after combustion of different types of coal. Process Saf. Environ. Prot. 133, 18–31.
Du, X.S., Tang, J.Y., Gao, X., Chen, Y.R., Ran, J.Y., Zhang, L., 2016. Molecular transformations of arsenic species in the flue gas of typical power plants: a density functional theory study. Energy Fuels 30, 4209–4214.
European Union Directive (EU), 2016. 2016/2284 of the European Parliament and of the Council of 14 December 2016 on the reduction of national emissions of certain atmospheric pollutants, amending Directive 2003/35/EC and repealing Directive 2001/81/EC. Off. J. Eur. Union 344, 1–31.
Finkelman, R.B., 2004. Potential health impacts of burning coal beds and waste banks. Int. J. Coal Geol. 59, 19–24.
Fu, B., Hower, J.C., Li, S., Huang, Y.D., Zhang, Y., Hu, H.Y., Liu, H.M., Zhou, J., Zhang, S. D., Liu, J.J., Yao, H., 2021. The key roles of Fe-bearing minerals on arsenic capture and speciation transformation during high-As bituminous coal combustion: experimental and theoretical investigations. J. Hazard. Mater. 415, 125610.
Haefeker, U., Kaindl, R., Tropper, P., Krüger, H., Kahlenberg, V., Orlova, M., 2014. Structural investigations of the two polymorphs of synthetic Fe-cordierite and Raman spectroscopy of hexagonal Fe-cordierite. Miner. Petrol. 108, 469–478.
Han, J.K., Yu, D.X., Wang, Q.Y., Yu, N., Wu, J.Q., Liu, Y., Luo, L., Pan, H.X., 2022. Beneficiation of coal ash from ash silos of six Chinese power plants and its risk assessment of hazardous elements for land application. Process Saf. Environ. Prot. 160, 641–649.
He, K.Q., Yuan, C.G., Shi, M.D., Jiang, Y.H., 2020. Accelerated screening of arsenic and selenium fractions and bioavailability in fly ash by microwave assistance. Ecotoxicol. Environ. Saf. 187, 109820.
Hu, P.B., Wang, S.J., Zhuo, Y.Q., 2021. Research on operation parameters and properties of flue gas on adsorption of As_2O_3 by γ-Al_2O_3: an experiment and simulation study. Process Saf. Environ. Prot. 152, 117–130.
Jerzak, W., Murzyn, P., Kuźnia, M., Magiera, A., 2021. Trace elements retention in bottom ashes during coal combustion with hydrated lime additions. Energy Sources Part A 43, 1215–1226.
Ji, P., Song, G.C., Xu, W.T., Song, Q., 2019. Transformation characteristics of arsenic and lead during coal combustion. Energy Fuels 33, 9280–9288.
Ling, Y., Li, J.C., Zou, C., Wu, J., Zhao, P.C., Xie, X.L., Qi, Y.F., Liu, Q.Z., Hong, J.D., Li, S., 2021. Interaction mechanism between gaseous arsenic and the unburned carbon in coal-fired fly ash: a DFT combined thermodynamics study. Chem. Eng. J. 425, 130714.
Press, W.H., Teukolsky, S.A., Vetterling, W.T., Flannery, B.P., 1996. Numerical Recipes in C, second ed. Cambridge University Press, Cambridge, UK.
Rahman, Z., Singh, V.P., 2019. The relative impact of toxic heavy metals (THMs) (arsenic (As), cadmium (Cd), chromium (Cr)(VI), mercury (Hg), and lead (Pb)) on the total environment: an overview. Environ. Monit. Assess. 191, 419.
Seames, W.S., Wendt, J.O.L., 2007. Regimes of association of arsenic and selenium during pulverized coal combustion. Proc. Combust. Inst. 31, 2839–2846.
Sefidari, H., Ma, C., Fredriksson, C., Lindblom, B., Wiinikka, H., Nordin, L.O., Wu, G., Yazhenskikh, E., Muller, M., Ohman, M., 2020. The effect of co-firing coal and woody biomass upon the slagging/deposition tendency in iron-ore pelletizing grate-kiln plants. Fuel Process. Technol. 199, 106254.
Shen, F.H., Liu, J., Zhang, Z., Dai, J.X., 2015. On-line analysis and kinetic behavior of arsenic release during coal combustion and pyrolysis. Environ. Sci. Technol. 49, 13716–13723.
Son, M.A., Chae, K.W., Kim, J.S., Kim, S.H., 2019. Crystal structure and thermal expansion coefficient of cordierite honeycomb ceramics. Phys. Status Solidi 216, 1700994.
Song, B., Yuan, K.P., Wei, Y.X., Chen, D.D., Meng, F.Y., Cao, Q., Song, M., Liu, H., 2021. In-furnace control of arsenic vapor emissions using Fe_2O_3 microspheres with good sintering resistance. Environ. Sci. Technol. 55, 8613–8621.
Song, G.C., Xu, W.T., Ji, P., Song, Q., 2019. Study on the transformation of arsenic and lead in pyrite during thermal conversion. Energy Fuels 33, 8463–8470.
Song, G.C., Xu, W.T., Liu, K., Song, Q., 2020a. Transformation of selenium during coal thermal conversion: effects of atmosphere and inorganic content. Fuel Process. Technol. 205, 106446.
Song, G.C., Xu, W.T., Yang, X.Y., Song, Q., 2022b. Retention of As during coal combustion: devolatilization and char combustion. Process Saf. Environ. Prot. 167, 203–212.
Song, G.C., Xu, W.T., Yang, X.Y., Song, Q., 2022c. Coupling effects of mineral components on arsenic transformation during coal combustion. J. Hazard. Mater. 435, 129040.
Song, G.C., Yang, X.Y., Li, Z.W., Song, Q., 2023. Adsorption mechanism of As_2O_3 by Ca-Si-Al mineral: an experimental and DFT study. J. Environ. Chem. Eng. 11, 110271.
Tian, H.Z., Zhu, C.Y., Gao, J.J., Cheng, K., Hao, J.M., Wang, K., Hua, S.B., Wang, Y., Zhou, J.R., 2015. Quantitative assessment of atmospheric emissions of toxic heavy metals from anthropogenic sources in China: historical trend, spatial distribution, uncertainties, and control policies. Atmos. Chem. Phys. 15, 10127–10147.
Tian, S.D., Fang, Y.X., Kang, Z.Z., Zhuo, Y.Q., 2015. Analysis of iron-bearing phase components in shenhua coal and their combustion transformation products by acid separation and Mossbauer spectroscopy methods. In: Yue, G., Li, S. (Eds.), Clean Coal Technology and Sustainable Development. ISCC. Springer, Singapore.
U.S. Environmental Protection Agency, 2012. National Emission Standards for Hazardous Air Pollutants from Coal and Oil–fired Electric Utility Steam Generating Units and Standards of Performance for Fossil–fuel–fired Electric Utility, Industrial–commercial–institutional, and Small Industrial–commercial–institutional Steam Generating Units. Federal Register, pp. 9487–9488.
Vanderbilt, D., 1990. Soft self-consistent pseudopotentials in a generalized eigenvalue formalism. Phys. Rev. B Condens. Matter 41, 7892–7895.
Wang, J.W., Zhang, Y.S., Liu, Z., Gu, Y.Z., Norris, P., Xu, H., Pan, W.P., 2019. Coeffect of air pollution control devices on trace element emissions in an ultralow emission coal–fired power plant. Energy Fuels 33, 248–256.
Wen, C., Gao, X.P., Xu, M.H., 2016. A CCSEM study on the transformation of included and excluded minerals during coal devolatilization and char combustion. Fuel 172, 96–104.
Wierońska-Wiśniewska, F., Makowska, D., 2022. A. Strugała assessment of the applicability of Ca-based sorbents for arsenic removal from flue gases. Energy Fuels 36, 6959–6964.
Wu, D.W., Yang, Y.J., Liu, J., 2022. As_2O_3 capture from incineration flue gas by Fe_2O_3-modified porous carbon: experimental and DFT insights. Fuel 321, 124079.
Xu, W.T., Song, G.C., Hu, K.X., Song, Q., Yao, Q., 2021. The redistribution of arsenic during the interaction between high-temperature flue gas and ash. Fuel Process. Technol. 212, 106641.
Xu, W.T., Song, G.C., Yang, X.Y., Song, Q., Yao, Q., 2022. Study on the chemical adsorption of gaseous As_2O_3 by ash. Fuel 330, 125557.
Yu, S.H., Zhang, C., Ma, L., Fang, Q.Y., Chen, G., 2021. Insight into As_2O_3 adsorption characteristics by mineral oxide sorbents: experimental and DFT study. Chem. Eng. J. 420, 127593.
Yu, Y., Zhao, R.H., Li, X.Y., Chen, J., Dong, Y., 2022. Mechanism of CaO and Fe_2O_3 capture gaseous arsenic species in the flue gas: DFT combined thermodynamic study. Fuel 312, 122838.
Zha, J.R., Huang, Y.J., Xia, W.Q., Xia, Z.P., Liu, C.Q., Dong, L., Liu, L.Q., 2018. Effect of mineral reaction between calcium and aluminosilicate on heavy metal behavior during sludge incineration. Fuel 229, 241–247.
Zhang, K.H., Zhang, D.X., Zhang, K., Yan, C., 2016. Capture of gas-phase arsenic by ferrospheres separated from fly ashes. Energy Fuels 30, 8746–8752.
Zhang, Y., Liu, J., 2019. Density functional theory study of arsenic adsorption on the Fe_2O_3 (001) surface. Energy Fuels 33, 1414–1421.

Zhao, B., Chen, G., Qin, L.B., Han, Y.X., Zhang, Q., Chen, W.S., Han, J., 2021. Effect of coal blending on arsenic and fine particles emission during coal combustion. J. Clean. Prod. 311, 127645.

Zhao, S.L., Duan, Y.F., Chen, L., Li, Y.N., Yao, T., Liu, S., Liu, M., Lu, J.H., 2017. Study on emission of hazardous trace elements in a 350 MW coal–fired power plant. Part 2. arsenic, chromium, barium, manganese, lead. Environ. Pollut. 226, 404–411.

Zhou, C.C., Liu, G.J., Xu, Z.Y., Sun, H., Lam, P.K.S., 2017. Effect of ash composition on the partitioning of arsenic during fluidized bed combustion. Fuel 204, 91–97.